EES Batteries

ROYAL SOCIETY OF CHEMISTRY

PAPER

View Article Online
View Journal | View Issue

Cite this: *EES Batteries*, 2025, **1**, 640

Superior sulfur infiltration into carbon mesosponge *via* chemical reaction for enhanced cycling stability in lithium–sulfur batteries†

Tianshu Liu,[a] Koki Fujita,[a] Ayako Kawase,*[b] Zheng-Ze Pan,[c] Takuma Kuroda,[d] Shinichiroh Iwamura[c,d] and Hirotomo Nishihara *[a,c]

Received 28th February 2025,
Accepted 25th April 2025

DOI: 10.1039/d5eb00039d

rsc.li/EESBatteries

Sulfur is a promising cathode material for secondary batteries, but its insulating nature and volume expansion during lithiation require encapsulation within carbon scaffolds. Moreover, the pronounced polysulfide shuttle effect hinders cycle stability. These issues make it difficult to achieve a sulfur content exceeding 70 wt% in typical sulfur–carbon composites, which are demanded for practical applications. This study explores a new scaffold, carbon mesosponge (CMS), featuring a single-layer graphene structure and a high mesopore volume of 3.01 $cm^3\ g^{-1}$. This unique structure allows for a sulfur content of up to 79 wt%. The S/CMS composite demonstrates superior cycling performance compared to conventional carbon scaffolds, such as KOH-activated carbon and graphene oxide. Additionally, two sulfur loading methods, physical and chemical, are compared. The chemical method facilitates sulfur deposition predominantly within the CMS pores, improving sulfur confinement and enhancing cycling stability compared to the physical method. This controlled sulfur deposition is attributed to the higher concentration of oxygen-functional groups within CMS pores, which could attract Na_2S_4, a precursor of sulfur. When used as the active material, the S/CMS composite prepared by the chemical method achieved a discharge capacity exceeding 1200 mA h g^{-1} in a pouch cell. This research underscores the importance of CMS as a scaffold and the superior sulfur-loading method in enhancing the performance of Li–S batteries.

Broader context

Lithium–sulfur batteries are emerging as a highly promising alternative to conventional lithium-ion batteries due to their high theoretical energy density and the natural abundance of sulfur. However, challenges such as rapid capacity decay, polysulfide dissolution, and poor sulfur utilization limit their practical application. This study addresses these fundamental limitations by developing a novel mesoporous carbon scaffold with tailored pore structures and oxygen-functionalized pore surfaces, enabling enhanced sulfur confinement and improved electrochemical stability. Moreover, our systematic investigation of sulfur loading strategies reveals that the chemical reaction method effectively anchors sulfur within the scaffold's pores, significantly suppressing the polysulfide shuttle effect compared to conventional melt diffusion methods. By emphasizing the importance of selecting appropriate carbon scaffolds and the effectiveness of chemical reaction techniques for sulfur loading, this research contributes to the advancement of high-performance Li–S batteries, thereby supporting the transition to cleaner and more sustainable energy solutions.

Introduction

Enhancing the performance of secondary batteries, especially achieving high energy density and prolonged cycle life, is essential to meet the growing demand for energy storage. While a mass-produced battery combining a high-capacity NCM ($LiNi_xCo_yMn_{1-x-y}O_2$) cathode with a silicon-based anode has recently achieved 360 W h kg^{-1}, the demand for even higher energy density is expected to increase further.[1] Thus, various types of advanced batteries have been extensively investigated.[2–5] One of the promising candidates is the Li–S battery. The sulfur cathode offers a theoretical specific capacity of up to 1672 mA h g^{-1}, and Li–S batteries can achieve an energy density up to 700 W h kg^{-1}.[6–8] Furthermore, its cost-effectiveness and abundant availability position sulfur as a promising candidate for future applications.[9] The Li–S battery is based on the redox reaction: $S_8 + 16Li^+ + 16e^- \leftrightarrow 8\ Li_2S$,

[a]*Institute of Multidisciplinary Research for Advanced Materials, Tohoku University, 2-1-1 Katahira, Aoba-ku, Sendai, Miyagi, 980-8577, Japan. E-mail: hirotomo.nishihara.b1@tohoku.ac.jp*
[b]*ENAX Inc., Tokyo, 112-0003, Japan. E-mail: ayakokawases@gmail.com*
[c]*Advanced Institute for Materials Research (WPI-AIMR), Tohoku University, 2-1-1 Katahira, Aoba-ku, Sendai, Miyagi, 980-8577, Japan*
[d]*3DC Inc., Sendai, Miyagi, 980-8577, Japan*
† Electronic supplementary information (ESI) available. See DOI: https://doi.org/10.1039/d5eb00039d

involving the generation of intermediate lithium polysulfide species.[10,11] This unique electrochemical process presents several challenges, including the insulating nature of sulfur and lithium sulfide, large volume expansion after cathode lithiation (up to 80%),[6] and the shuttle effect of polysulfides, leading to continuous active material loss and low coulombic efficiency.[10,12] To overcome these obstacles, considerable efforts have been made towards the optimization of electrolyte additives,[13,14] binder materials,[15,16] electrocatalysts[17,18] and especially sulfur host materials.[19–23] Carbon materials are typically used as sulfur host materials due to their excellent electric conductivity, lightweight properties, mechanical properties, and chemical stability.[24–26] Among various types of carbon materials, carbon nanofiber,[27] graphene-based materials,[22,28] and porous carbons[29,30] have received significant attentions as sulfur supports, because of their superior electrical conductivity and ability to confine sulfur effectively.[31] Nevertheless, the sulfur content in most sulfur–carbon composites typically remains below 70 wt%, due to the more severe shuttle effect and reduced conductivity observed in electrodes with higher sulfur loading. Additionally, carbon materials must have sufficient pore volume to accommodate volume expansion of sulfur, but achieving high pore volume while maintaining good electrical conductivity remains challenging. These factors significantly impact Li–S batteries in achieving higher energy density and longer cycle life compared to commercialized lithium-ion batteries.[7] Therefore, it is highly demanded to develop novel carbon host materials that can address the aforementioned challenges.

To fully maximize the potential of the carbon host, it is also important to carefully consider the method of sulfur incorporation. The most widely used method is a physical approach, melt-diffusion, where a carbon–sulfur mixture is heated above the melting point of sulfur in an inert atmosphere, allowing molten sulfur to penetrate the carbon pores.[32–34] However, some studies have noted a tendency that sulfur often accumulates on the carbon surface rather than diffusing efficiently into the pores, which compromises sulfur confinement and leads to rapid capacity decay.[35] On the other hand, the chemical approach, which involves the conversion of a sulfur-containing precursor into sulfur, is expected to achieve more uniform loading, particularly into carbon pores where precursor concentration tends to increase due to adsorption.[36] Commonly used precursors include sodium thiosulfate ($Na_2S_2O_3$),[37,38] sodium polysulfide (Na_2S_x),[39,40] and sulfur-ethylenediamine (S-EDA).[41] Through well-controlled reaction conditions, the particle size of sulfur can be reduced, beneficial for achieving a large contact area between carbon and sulfur and a short ion diffusion length of Li^+ inside sulfur/carbon composites.

Although extensive research has been conducted on Li–S batteries, challenges remain in developing the high-performance carbon material as sulfur host along with the efficient method for sulfur deposition. In this study, we explore the feasibility of a new mesoporous carbon scaffold, called carbon mesosponge (CMS), and an optimal sulfur-loading method. CMS can be synthesized through a template carbonization method,[42,43] using CH_4 as the carbon source for chemical vapor deposition (CVD).[44,45] CMS exhibits a high volume of mesopores, which serve as reservoirs to accommodate sulfur expansion and enable the physical adsorption of lithium polysulfide within these pores. Significantly, CMS is primarily composed of quasi-single-layer graphene walls with defects, which offers significant mechanical flexibility.[46] Moreover, the defective pore walls of CMS contain oxygen-functional groups that are beneficial for chemically trapping lithium polysulfide within the cathode.[47] The capacity retention of S/CMS composites outperforms the counterpart materials prepared by those reported sulfur hosts including MAXSORB (KOH-activated carbon)[48] and graphene oxide (GO).[49] To maximize the potential of CMS as the sulfur support material, two sulfur loading methods, physical melt-diffusion and chemical reaction, were examined. It is found that the chemical method provides sulfur loading mostly inside CMS pores, which contributes to improved capacity retention. Moreover, the pouch cell using the S/CMS composite prepared through the chemical reaction method demonstrated a discharge capacity of approximately 1200 mA h g^{-1} after 30 cycles. This study highlights the importance of selecting carbon scaffold and the effectiveness of chemical reaction method for sulfur loading in achieving high-performance Li–S batteries.

Results and discussion

Properties of sulfur hosts and the procedure of sulfur loading

In this study, three types of carbon hosts are examined (Fig. 1a–c and S1a–c†). Activated carbons (ACs) are the most popularly used sulfur-host materials,[50,51] and we have selected the one with a developed porosity *via* KOH-activation (Fig. 1a and S1a†). The AC possesses a high BET specific surface area (S_{BET}) of 2546 m^2 g^{-1} and a large total pore volume (V_{total}) of 1.64 cm^3 g^{-1} (Fig. S2a†), with its pore size ranging from 1 to 3 nm (Fig. S2b†). Graphene oxide (GO; Fig. 1b and S1b†) has been also used as a sulfur host,[52] and we employ it as a counterpart in this study. GO has a limited porous structure showing a S_{BET} of 19 m^2 g^{-1} (Fig. S2c and d†), but rich in oxygen-functional groups. CMS (Fig. 1c and S1c†) exhibits a two-dimensional nanoplate-shaped particle morphology with a lateral size of less than 1 μm and a thickness of less than 100 nm. This structure promotes efficient ion diffusion within the particles and improves electron transfer through planar contact between individual particles and with current collector.[42] CMS can be synthesized *via* CVD on a porous MgO template, followed by template removal using aqueous HCl. After the HCl treatment and rinsing with pure water, the wet CMS, referred to as wCMS, is obtained. By replacing the water with acetone and drying at 150 °C, CMS is obtained. In this study, wCMS and CMS are used for chemical and physical sulfur impregnation, respectively. Depending on the solvent used during the drying process, mesopore shrinkage can occur due to capillary forces. Fig. S2e† displays the nitrogen adsorption–

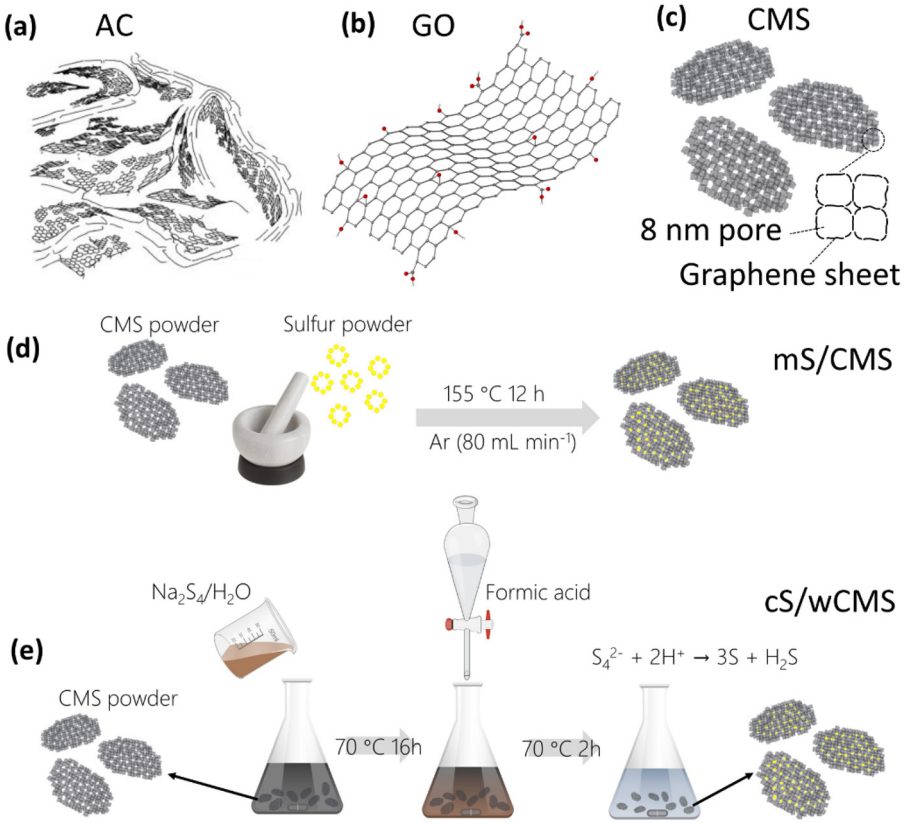

Fig. 1 Carbon materials utilized in this study. (a) Activated carbon (AC). (b) Graphene oxide (GO). (c) Carbon mesosponge (CMS). (d and e) The preparation scheme of S-loaded samples. (d) Melt diffusion method. (e) Chemical reaction method.

desorption isotherms of water-dried CMS and acetone-dried CMS, which represent the porosities of wCMS and CMS, respectively, in the hypothetical absence of sulfur in their S-loaded forms, respectively. Both isotherms indicate a highly mesoporous structure with an uptake and hysteresis observed above P/P_0>0.4. The S_{BET} and V_{total} of water-dried CMS are 1921 $m^2\ g^{-1}$ and 3.01 $cm^3\ g^{-1}$, and those for acetone-dried CMS are 2128 $m^2\ g^{-1}$ and 3.63 $cm^3\ g^{-1}$, respectively. The pore-size distributions show peak pore size at 8.1 nm for wCMS, smaller than that of CMS at 8.3 nm (Fig. S2f†). Fig. 1d and e illustrate the methods of sulfur loading onto CMS and wCMS, respectively. The melt diffusion method (Fig. 1d) involves physically mixing CMS and sulfur powder, followed by a heat treatment at 155 °C for 12 h under an Ar atmosphere. The resulting composite is referred to as mS(X)/CMS, where "m" denotes the melt-diffusion method, and "X" represents the sulfur loading amount (wt%) in the composite. The chemical reaction method (Fig. 1e) consists of two steps: introducing Na_2S_4 into the wCMS/water dispersion to generate sulfur seed crystals, followed by adding formic acid to accelerate sulfur deposition into the wCMS.[39] The resulting composite, referred to as cS(X)/wCMS, is obtained by drying the water under 60 °C, where "c" denotes the chemical reaction method. Similarly, sulfur is loaded into AC and GO using the melt diffusion and chemical reaction methods. The resulting samples are named in the same manner as those for CMS and wCMS, with CMS or wCMS replaced by AC or GO.

Properties of sulfur/carbon composites

The thermogravimetric analysis (TGA) curves of the sulfur/carbon composites under a nitrogen atmosphere are displayed in Fig. 2a. The sulfur content of each sample is estimated from the total weight loss after heating to 500 °C. Sulfur was loaded at 79 wt% onto the wCMS, CMS, and AC supports, and at 86 wt% onto the GO support. The morphology of the sulfur/carbon composites, as shown in Fig. S1d–i†, exhibits no significant differences across the various sulfur loading methods. Additionally, the elemental mapping of each composite (Fig. S3†) illustrates a homogeneous sulfur distribution, at least the measurement resolution (approximately a few micrometers). The derivative weight loss *versus* temperature (dW/dT) curves (Fig. 2b) obtained from TGA analysis provide deep insights into the sulfur distribution within the composites.[51]

The dW/dT curve for pure sulfur powder shows evaporation starting around 170 °C and reaching its maximum rate around 310 °C. The evaporation profiles of S/GO composites closely resemble that of pure sulfur, indicating that most sulfur is not confined within nanopores. In contrast, the dW/dT curves for S/AC composites exhibit two distinct peaks, where the first

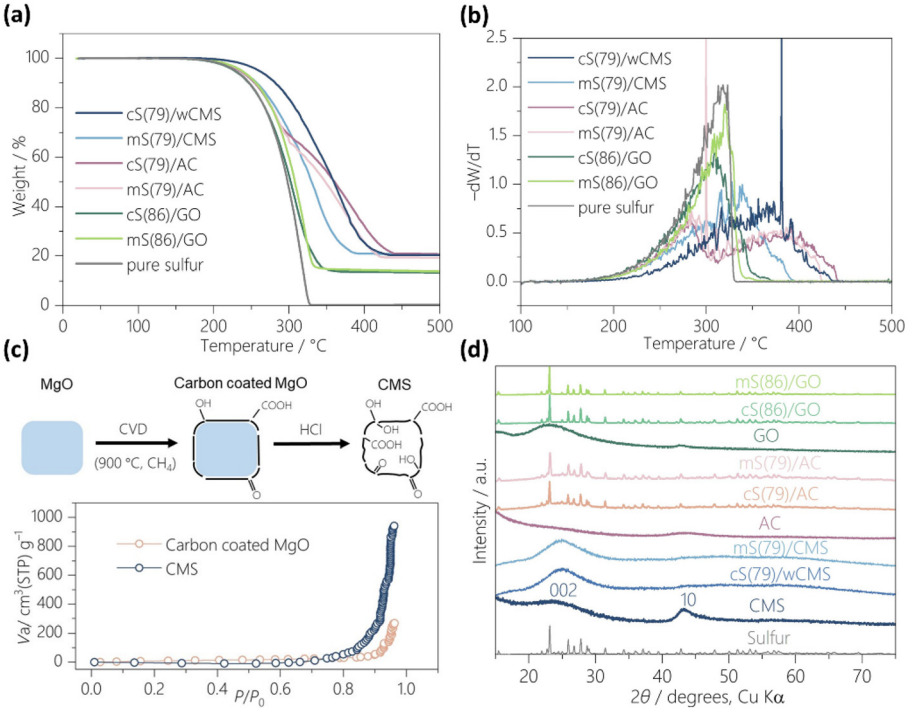

Fig. 2 Analysis of sulfur loaded on carbon scaffolds. (a) TG curves of sulfur/carbon composites under nitrogen atmosphere. (b) Derivative weight loss *versus* temperature obtained from TGA results. (c) Preparation scheme of CMS (top) and water vapor adsorption isotherms of CMS before and after template removal (bottom). (d) XRD patterns.

peak appears below 300 °C, and a second peak around 400 °C. This behavior is likely due to AC's limited pore volume; with 79 wt% sulfur loading, the composite exceeds its maximum pore volume at 111%. Specifically, 1 g of AC accommodates 3.76 g of sulfur, exceeding its maximum capacity of 3.39 g of sulfur per gram of AC (Table S1†). So, the first peak represents sulfur loss from the AC surface, while the second peak arises from sulfur confined within the small pores less than 3 nm.

The dW/dT curve of mS(79)/CMS shows a similar profile to S/GO and S/AC below 300 °C, which can be attributed to unconfined sulfur. The curve segment above 300 °C corresponds to sulfur within mesopores, though this peak occurs at a lower temperature than the second peak in S/AC. Although the pore volume of CMS is sufficient to accommodate 7.51 g of sulfur per gram of CMS, the actual sulfur content is 3.76 g per gram of CMS, representing only 50% of its capacity (Table S1†). However, the sulfur distribution remains uneven across the mesopores. In contrast, cS(79)/wCMS exhibits the highest sulfur evaporation onset temperature exceeding 200 °C and a peak weight loss at 380 °C, indicating that sulfur is effectively confined within the wCMS pores. In this composite, 1 g of wCMS accommodates 3.76 g of sulfur, utilizing 60% of its total pore volume, with a maximum capacity of 6.23 g of sulfur per gram of wCMS (Table S1†). The effective sulfur confinement observed in wCMS is attributed to the presence of oxygen-functional groups within its mesopores, which enhance the adsorption of the polar sulfur precursor, Na_2S_4. This is supported by the comparative results shown in Fig. S4,† where Na_2S_4 adsorption tests and UV–vis measurements were conducted using CMS and GMS. GMS shows a similar porous structure to CMS, but it is free of edge sites as a result of high temperature annealing at 1800 °C, as reported in our previous work.[47] When CMS was added into the aqueous Na_2S_4 solution, the solution gradually turned colorless, whereas it remained yellow when the same amount of GMS was introduced. Furthermore, the characteristic absorption peak of S_4^{2-} at 410 nm in UV-vis spectra significantly reduced in Na_2S_4/CMS, compared to both the pure Na_2S_4 solution and the Na_2S_4/GMS, indicating stronger interaction between oxygen-functional groups of CMS and Na_2S_4.[53] More importantly, the uneven distribution of oxygen-functional groups is generally observed in the template method, as shown in the top illustration of Fig. 2c.[54] When a carbon coating is applied to the template *via* CVD, non-terminated edge sites are present at the interface between the carbon layer and the template. Upon removal of the template, these edge sites become oxidized, resulting in the introduction of a large number of oxygen-functional groups.[55] As shown in the bottom of Fig. 2c, water-vapor adsorption amount of CMS is much larger than its precursor, indicating that oxygen-functional groups are predominantly present on the surfaces of mesopores formed after the removal of the template. During the synthesis of cS(79)/wCMS, these polar functional groups attract polar sodium polysulfides, promoting sulfur deposition within the pores.

Fig. 2d shows the XRD profiles of pure carbons and sulfur/carbon composites. Pure CMS shows the 10 peak around 44°,

corresponding to the in-plane diffraction of a planar graphene sheet.[56] The broad and weak 002 peak around 26° suggests rare stacking of the graphene layers.[44,47] As a reference, a S/CMS composite with 79 wt% sulfur was prepared by a physical mixing of sulfur powder and CMS powder, referred to as pS (79)/CMS, where "p" denotes the physical mixing. The XRD profile of pS(79)/CMS shows intense characteristic sulfur peaks (Fig. S5†). In contrast, in mS(79)/CMS and cS(79)/wCMS, multiple sulfur peaks in the 20–30° range appear as a single broad peak, suggesting that the sulfur is supported in the form of small clusters. On the other hand, the XRD profiles for sulfur-loaded AC or GO, regardless of the sulfur loading method, display sharp sulfur peaks, indicating that a significant amount of crystalline sulfur is deposited in these carbon scaffolds. The maximum sulfur content within the carbon scaffolds is calculated under the assumption that the carbon pores are fully filled with sulfur (Table S1†). The value for AC and GO are 77 wt% and 7 wt%, respectively, with a sulfur loading of 79 wt% exceeding their maximum capacity. In contrast, the maximum sulfur content for the CMS and wCMS is significantly higher, at 88 wt% and 86 wt%. Thus, CMS and wCMS can serve as high-capacity sulfur scaffolds.

Raman spectrum (Fig. S6†) of CMS shows the G band, corresponding to the E_{2g} symmetry of graphene, along with an intense D band, arising from abundant functional groups and topological defects.[47,57] In the spectrum of cS(79)/wCMS and mS(79)/CMS, the specific sulfur peaks locating between 100 cm^{-1} to 500 cm^{-1} are absent, suggesting sulfur encapsulated in the CMS scaffold, as also evidenced by XRD results. The intensity ratio (I_D/I_G) of D band and G band in CMS is not significantly changed before (1.87) and after (1.69) sulfur loading, indicating that the sulfur loading does not alter the intrinsic structure of CMS and preserves its high electrical conductivity for efficient electron transfer.[58] In contrast, both S/AC and S/GO composites are observed with characteristic sulfur peaks.

Effects of sulfur loading methods on porous structures of sulfur/CMS composites are also investigated by N_2 adsorption as shown in Fig. S7.† Both S/CMS composites show a disappearance of uptake and hysteresis in their isotherms, compared to the results observed prior to sulfur loading (Fig. S2e and f†). Theoretically, V_{total} after loading 79 wt% sulfur, assuming no pore blocking, is expected to be 0.25 $cm^3\ g^{-1}$ for cS(79)/wCMS and 0.38 $cm^3\ g^{-1}$ for mS(79)/CMS. The measured values, 0.19 $cm^3\ g^{-1}$ and 0.28 $cm^3\ g^{-1}$, respectively, align well with these estimates.

Electrochemical properties of sulfur/carbon composites

The electrochemical properties of various sulfur/carbon composites were evaluated by using half-cell configurations, maintaining a consistent sulfur content of 60 wt% in the electrodes. The discharge–charge properties of the mS(79)/CMS and cS (79)/wCMS were evaluated through galvanostatic charge–discharge (GCD) measurements at various rates ranging from 1/40 C to 1/5 C (1 to 14 cycles), as shown in Fig. 3a and b, respectively. The initial two cycles at 1/40 C serve as a conditioning process. The 1st discharge capacities of mS(79)/CMS and cS(79)/wCMS were 1551 and 1499 mA h g^{-1}, respectively, whereas these values dropped to 1113 and 1190 mA h g^{-1}, respectively, at the 2nd discharge. At the rate of 1/20 C (3 to 6 cycles), cS(79)/wCMS exhibits higher discharge capacities, ranging from 971 to 1054 mA h g^{-1}, compared to mS(79)/CMS,

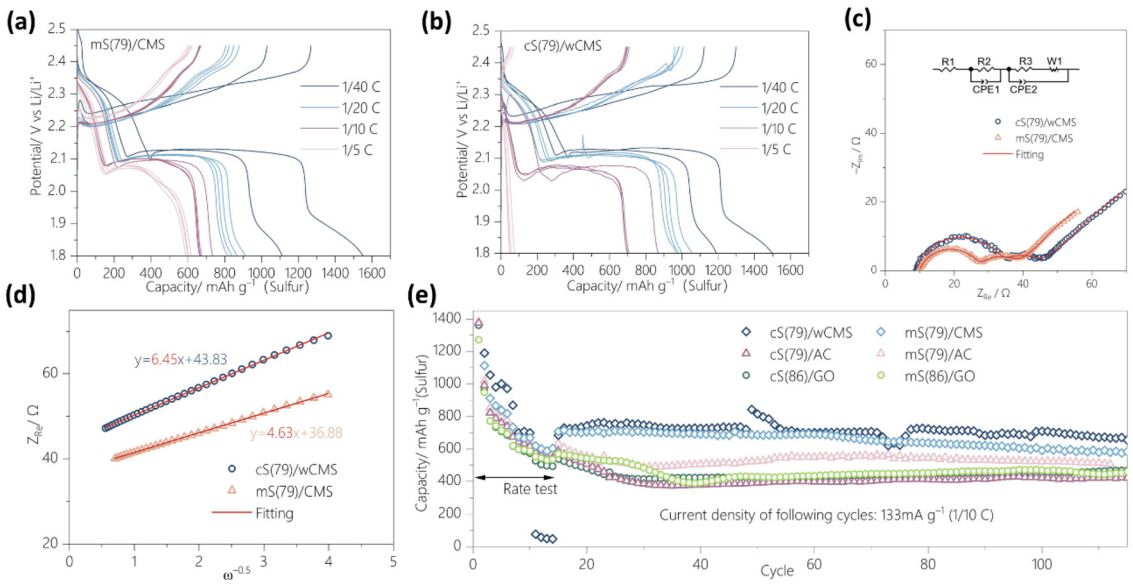

Fig. 3 Electrochemical properties of S/CMS composites. (a and b) GCD curves of (a) mS(79)/CMS and (b) cS(79)/wCMS under different rates. (c) Nyquist plots after cell discharging to 2.15 V. (d) The relationship between real part of impedance and the inverse square root of angular frequency. (e) Cycling stability performance. The initial 14 cycles were conducted at varying rates, as shown in a and b. Starting from the 15th cycle, a constant current density of 133 mA g^{-1} (1/10C) was applied. The electrolyte is 1 M LiTFSI + 1 M $LiNO_3$ + 0.08 M $La(NO_3)_3$ in DME/DOL.

which ranges from 818 to 912 mA h g^{-1}. At low discharge rates of 1/40 C and 1/20 C, both composites exhibit a flat discharge plateau around 2.1 V, corresponding to the reduction of Li_2S_4 to Li_2S_2. This is followed by a sloping region below 1.9 V, which is attributed to the subsequent conversion of Li_2S_2 to Li_2S.[59,60] When the discharge rate increases to 1/10 C (7 to 10 cycles), cS(79)/wCMS displays a pronounced potential 'dip' at the early stage of discharge, followed by a plateau at 2.08 V, indicating a significant barrier for the nucleation and initial growth of solid Li_2S_2/Li_2S,[61] while mS(79)/CMS shows a much smaller potential dip. Moreover, the absence of the sloping discharge region below 1.9 V in both composites suggests that Li_2S_2 is not fully converted into Li_2S. This is likely due to the limited electron transport across the insulating Li_2S_2/Li_2S and the high activation energy required for the solid to solid conversion, particularly under high current conditions.[62,63] At 1/5 C (11 to 14 cycles), the capacity of cS(79)/wCMS dramatically reduces to below 80 mA h g^{-1}, and the discharge curve shows a sharp potential drop without any plateau, indicating a large amount of sulfur remains unreduced to polysulfide.[61] In contrast, mS(79)/CMS maintains a discharge capacity of approximately 600 mA h g^{-1}. Electrochemical impedance spectroscopy (EIS) in Fig. 3c offers additional insights into the rate performance difference. Specifically, EIS was carried out after discharging cells to 2.15 V, where soluble polysulfides are formed, allowing analysis of ion diffusion resistance. The high frequency semi-circles are significantly reduced compared to those at pristine status before discharge (Fig. S8†), revealing reduced charge transfer resistance due to the transformation of solid sulfur to soluble polysulfide species.[64] To further investigate the lithium-ion diffusion inside the cathode, the real part of Warburg impedance against the square root of the angular frequency is fitted in Fig. 3d, with additional results from multiple cells presented in Fig. S9.† The mS(79)/CMS achieves a lower Warburg coefficient ranging from 4.06 to 4.97 $\Omega\ s^{-1/2}$, compared to 5.23 to 6.45 $\Omega\ s^{-1/2}$ for cS(79)/wCMS. Since both sulfur/CMS composites were subjected to similar electrochemical measurement conditions, their diffusion coefficients and Warburg coefficients are inversely proportional.[65] These results indicate that the ion diffusion coefficient of cS(79)/wCMS is lower than that of mS(79)/CMS.[66] These results indicate that pore blocking is more pronounced in cS(79)/wCMS, which impedes ion diffusion.

After the examination of the rate performance, cycling tests at 1/10 C (equivalent to 133 mA g^{-1}) were conducted, as shown in Fig. 3e. Both S/CMS composites obtain stable discharge capacities above 700 mA h g^{-1} when the discharge rate returns to 1/10 C from 1/5 C. To confirm the reproducibility, the cycling performance was further validated using multiple cells, as displayed in Fig. S10.† After 100 cycles, mS(79)/CMS achieves a capacity retention ranging from 553 to 611 mA h g^{-1}, while cS(79)/wCMS exhibits higher value between 577 and 709 mA h g^{-1}. Moreover, Fig. S11† shows the cycling results after 300 cycles, where cS(79)/wCMS maintains a higher discharge capacity of 557 mA h g^{-1} (76% retention), along with higher coulombic efficiency, compared to mS(79)/CMS, which achieves 481 mA h g^{-1} (67% retention). The superior cycling stability of cS(79)/wCMS can be attributed to the pronounced sulfur confinement within the scaffold. Additionally, the presence of abundant oxygen-functional groups within wCMS nanopores can effectively attract polysulfide species, preventing their diffusion and inhibiting continuous sulfur loss. Conversely, mS(79)/CMS, with less sulfur confined in the mesopores, experiences fewer limitations on lithium-ion diffusion but suffers from more significant active material loss during cycling. For comparison, sulfur/carbon composites prepared with AC and GO underwent the same cycling tests, showing rapid capacity decay to below 550 mA h g^{-1} after 100 cycles. For GO, which is poor in nanopores, there is no performance difference between melt diffusion and chemical reaction methods. For AC, with hydrophobic nanopores smaller than 3 nm, the melt diffusion method yields better results, while in CMS, with hydrophilic nanopores between 3 and 15 nm, the chemical reaction method is more effective. These results emphasize the superior capacity retention of CMS compared to other carbon materials and demonstrate that hydrophilic CMS nanopores are well-suited for sulfur deposition through chemical reactions.

Despite employing the same carbon scaffold, different synthesis methods result in substantial differences in rate performance and cycling stability. SEM images of mS(79)/CMS and cS(79)/wCMS electrodes at pristine status and after one cycle of GCD are shown in Fig. 4a–d. At the pristine status, both electrodes show a mixture of S/CMS particles and homogeneously distributed carbon nanotubes (CNTs) as electrically conductive additives (Fig. 4a and c). After one GCD cycle, a solid deposit, ascribed to sulfur, covers the surface of the mS(79)/CMS electrode, rendering the CNTs invisible (Fig. 4b). This indicates sulfur deposition outside the nanopores of CMS. In contrast, the cS(79)/wCMS electrode retains its morphology, indicating that sulfur particles are still confined within wCMS pores (Fig. 4d). These differences become more pronounced after 100 cycles. The mS(79)/CMS electrode exhibits an uneven distribution of sulfur or lithium sulfide, with noticeable voids between interconnected deposits. These non-conductive deposits hinder lithium-ion diffusion and electron transport, leading to incomplete electrochemical reactions (Fig. S12a†).[67] In contrast, the cS(79)/wCMS electrode exhibits a denser surface morphology while retaining the distinct structure of the original wCMS particles (Fig. S12b†), indicating superior structural stability and electrical conductivity throughout cycling.

When sulfur transforms into lithium sulfide, it expands in volume. Therefore, an additional space should be provided around the sulfur in the sulfur/carbon composites.[68] When assuming that all the sulfur is confined within the mesopores of mS(79)/CMS, the volume of sulfur and expanded lithium sulfide accounts for 50% and 89% of CMS's total pore volume, respectively (Table S2†). However, as discussed above, a significant portion of sulfur is actually deposited outside the CMS mesopores (Fig. 4e). This deposition behavior leaves sufficient space within mesopores, facilitating the diffusion of polysulfides during cycling. Consequently, sulfur redeposits outside

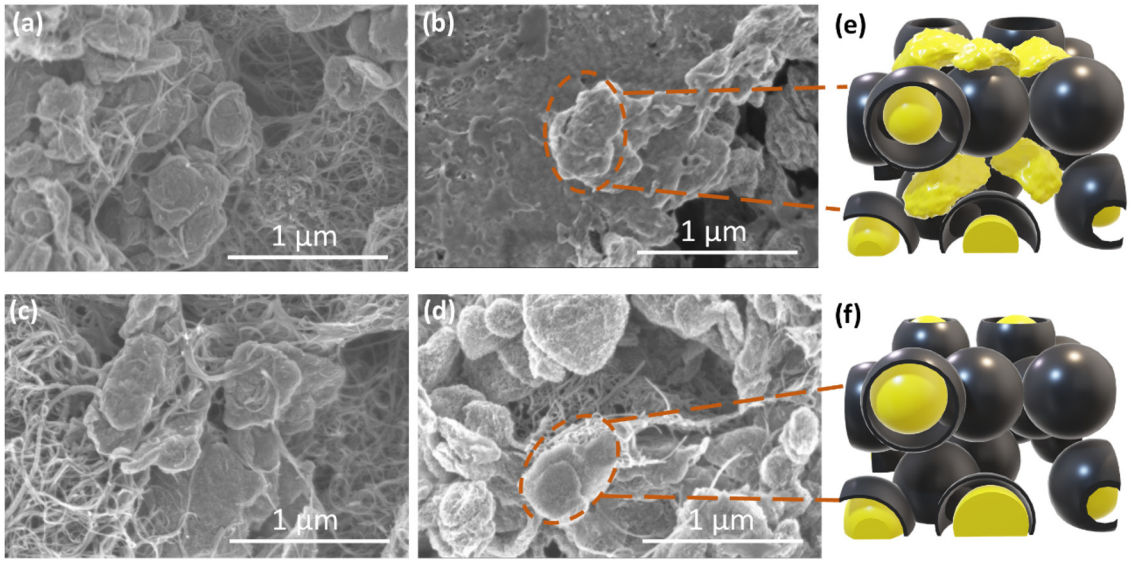

Fig. 4 Electrode morphology of different S/CMS composites. (a and b) SEM images of mS(79)/CMS. (a) Pristine status. (b) After one cycle discharge–charge. (c and d) SEM images of cS(79)/wCMS. (c) Pristine status. (d) After one cycle discharge–charge. (e and f) Illustration showing sulfur and lithiated sulfur in (e) mS(79)/CMS and (f) cS(79)/wCMS.

the mesopores during charging, contributing to reduced resistance to lithium-ion diffusion within the pores. On the other hand, the sulfur content in cS(79)/wCMS is 79 wt%, which corresponds to 60% of the total pore volume of wCMS (Table S2†). Upon full lithiation, the volume of sulfur expands to 108% of the total pore volume of wCMS. This suggests that the mesopores could become blocked during lithiation, leaving limited space for polysulfides to diffuse or escape. This confinement results in sluggish reaction kinetics, particularly at high current densities (Fig. 4f).

Optimization of sulfur-loading amount

Based on the discussion on Fig. 4f, the sulfur content in the sulfur/CMS composites was further optimized to 73 wt%, while maintaining a same sulfur content of 60 wt% in the electrodes by adjusting the CNTs ratio. In the resulting cS(73)/wCMS composite, sulfur and lithiated sulfur occupy 43% and 78% of wCMS's total pore volume, respectively (Table S2†), ensuring that sufficient pores are available for ion diffusion throughout the charge–discharge processes. The GCD properties of mS(73)/CMS and cS(73)/wCMS were evaluated at high rates ranging from 1/10 C to 1 C, as displayed in Fig. 5a and b, respectively, with the corresponding rate performance summarized in Fig. 5c. At 1/10 C, the discharge capacities of mS(73)/CMS range from 1387 to 965 mA h g^{-1}, comparable to those of cS(73)/wCMS ranging from 1436 to 1022 mA h g^{-1}. When the rate increases to 1/5 C, cS(73)/wCMS demonstrates improved performance, with discharge capacities ranging from 924 mA h g^{-1} to 765 mA h g^{-1}, outperforming mS(73)/CMS ranging from 858 mA h g^{-1} to 646 mA h g^{-1}. In contrast to the case of cS(79)/wCMS (Fig. 3b), the GCD curves of cS(73)/wCMS at 1/5 C exhibit a discharge plateau without a significant potential 'dip', suggesting improved reaction kinetics. This is due to the optimization of sulfur content, which maintains sufficient diffusion pathway. Moreover, at higher rates such as 1/2 C and 1 C, cS(73)/wCMS maintains competitive performance, achieving discharge capacities of 548 to 413 mA h g^{-1} at 1/2 C, and 268 to 200 mA h g^{-1} at 1 C. In contrast, mS(73)/CMS significantly underperforms at these rates, with capacities falling below 170 mA h g^{-1} at 1/2 C and below 22 mA h g^{-1} at 1 C. Additionally, rate performance across multiple cells in Fig. S13† highlight the enhanced high-rate capability of cS(73)/wCMS compared to mS(73)/CMS. Cycling stability tests at a constant rate of 0.1 C are presented in Fig. 5d, along with reproducibility results shown in Fig. S14.† The cS(73)/wCMS undergoes an aging process before 30 cycles, stabilizing at a capacity of 785 mA h g^{-1}. This initial capacity drop is attributed to the high electrolyte-to-sulfur (E/S) ratio of 20 μL mg^{-1}, which promotes the dissolution of lithium polysulfides into the electrolyte and making more sever shuttle effect.[67] The cS(73)/wCMS maintains a capacity of 695 mA h g^{-1} after 120 cycles, significantly outperforming mS(73)/CMS, which retains 493 mA h g^{-1} after the same number of cycles. As shown in Fig. 5e, the GCD curves of cS(73)/wCMS from the 30th to the 100th cycle exhibit longer discharge plateaus in both the 1st and 2nd stages compared to mS(73)/CMS, indicating stable sulfur utilization over the cycles. Furthermore, the dQ/dV curves derived from GCD measurements are displayed in Fig. S15,† showing a reduction peak around 2.1 V and oxidation peak around 2.2 V. For mS(73)/CMS, the overpotential between these peaks is 141.6 mV at 30th cycle, increasing by 14.5 mV at 100th cycle (Fig. S15a†). In comparison, cS(73)/wCMS exhibits a lower overpotential of 131.6 mV at 30th cycle, with a smaller increase of 5.7 mV at 100th cycle (Fig. S15b†). This smaller overpotential increase for cS(73)/wCMS indicates higher reversibility of the electrochemical reaction compared

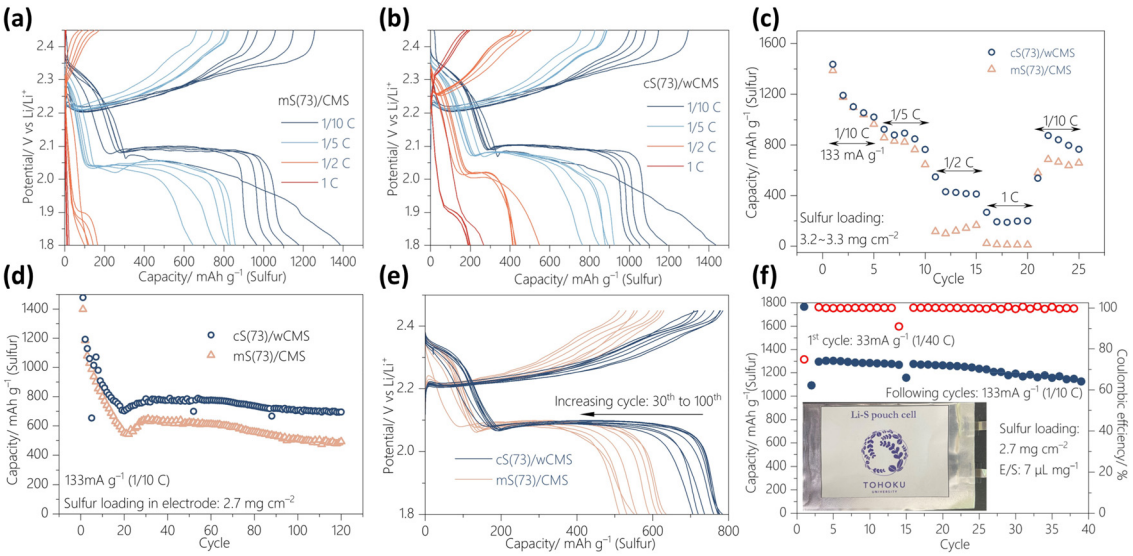

Fig. 5 Electrochemical measurements of S/CMS composites with an optimized sulfur content (73 wt%). (a and b) GCD curves of (a) mS(73)/CMS and (b) cS(73)/wCMS under different rates. (c) Rate performance. (d) Cycling stability. (e) GCD curves during cycling tests. (f) Cycling test of a pouch cell using cS(73)/wCMS.

to mS(73)/CMS. To explore the industrial potential of Li–S batteries, the high-performance cS(73)/wCMS electrode was used to assemble a pouch cell with a cathode size of 12 cm^{-2} (Fig. S16†). The cell demonstrated outstanding capacity retention, maintaining approximately 1200 mA h g^{-1} after 30 cycles (Fig. 5f). It is worth noting that the pouch cell demonstrates even better capacity retention compared to the coin cell. This improvement can be attributed to its lower E/S ratio at 7 μL mg^{-1}, which is significantly lower than the case in the coin cell. The reduced electrolyte amount limits polysulfide dissolution, keeping more active sulfur within the cathode and thereby mitigating initial capacity loss.[69] To support this explanation, a coin cell was assembled with an E/S ratio of 7 μL mg^{-1}, which demonstrated improved capacity retention during the first 20 cycles (Fig. S17†). The pouch cell achieved an energy density of 175 W h kg^{-1}, calculated based on the total weight of the cathode, anode, separator and electrolyte (supporting calculation 1), which falls short of meeting practical application requirements. To achieve energy densities exceeding 350 W h kg^{-1}, reducing the E/S ratio below 3 μL mg^{-1} is crucial, potentially using advanced sparingly solvating electrolytes.[70] Nevertheless, the capacity retention of the pouch cell developed in this study surpasses that of previously reported lithium–sulfur pouch cells (Table S3†). We emphasize this study focuses on advancing sulfur cathodes with pure carbon scaffolds, avoiding costly metal catalysts, and utilizing conventional organic electrolytes. These findings demonstrate that selecting CMS as the carbon scaffold and utilizing chemical reactions for sulfur loading hold promising potential for achieving high energy density Li–S batteries, particularly when employed with advanced electrolyte systems.

During the sulfur reduction process, soluble polysulfide species can diffuse to the anode and chemically react with lithium metal, forming a solid electrolyte interface (SEI) on the lithium surface. Over repeated cycles, this SEI becomes loose and highly porous, accelerating the depletion of lithium metal and electrolyte, which leads to the formation of a thicker SEI

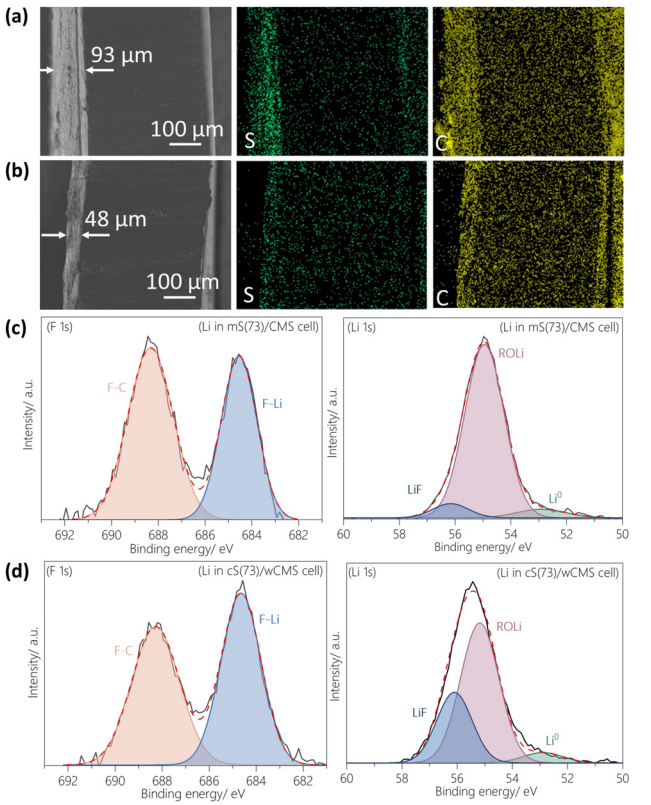

Fig. 6 Lithium anode characterization of different S/CMS composites included cells. (a and b) SEM images and elemental mapping of lithium anode cross section. (a) mS(73)/CMS. (b) cS(73)/wCMS. (c and d) XPS spectra of lithium anode. (c) mS(73)/CMS. (d) cS(73)/wCMS.

layer. This continues reaction between polysulfides and lithium metal is known as sulfur crosstalk.[71] Fig. 6a and b display the SEM cross-sectional morphologies of the lithium anodes after 120 cycles. The SEI layer in the mS(73)/CMS cell is 93 μm thick, compared to 48 μm in the cS(73)/wCMS cell. Elemental mapping shows that the lithium surface of the mS (73)/CMS cell has higher sulfur and carbon signals than that of the cS(73)/wCMS cell. X-ray photoelectron spectroscopy (XPS) results in Fig. 6c and d provide further insight into the SEI composition. The F 1s spectra reveal peaks at 684.6 eV and 688.3 eV, corresponding to F–Li and F–C, respectively. The cS (73)/wCMS cell's lithium anode shows a more intense F–Li peak relative to the F–C peak. Additionally, the Li 1s spectra for the cS(73)/wCMS cell's lithium anode is shifted left compared to the mS(73)/CMS cell's lithium anode, indicating a stronger Li–F peak in the SEI layer. These observations suggest that a higher content of inorganic SEI is formed on the cS(73)/wCMS cell's lithium anode. The restricted growth of this inorganic-enriched SEI layer in the cS(73)/wCMS cell's lithium anode indicates that polysulfide species are largely confined within wCMS pores, effectively inhibiting the shuttle effect and sulfur crosstalk on the lithium anode.

Conclusions

In this research, a mesoporous carbon CMS was applied as the sulfur host material for the Li–S battery. CMS exhibits a large pore volume at 3.01 $cm^3\ g^{-1}$ and a peak pore size of approximately 8 nm, which enables sufficient space for sulfur expansion. The synthesized S/CMS composites show better cycling stability performance than its counterpart composites prepared by AC and GO. Additionally, the influence of sulfur loading methods on the performance of S/CMS composites was investigated. By comparing chemical reaction and melt diffusion methods, it was found that the chemical reaction method resulted in superior sulfur confinement within the wCMS pores, leading to enhanced cycling stability and overall electrochemical performance. The pouch cell assembled with cS(73)/wCMS achieved 1200 mA h g^{-1} after 30 cycles, demonstrating its practical applicability. This work highlights that the choice of sulfur loading method significantly affects the electrochemical performance in Li–S batteries, with the chemical reaction method proving to be superior in the case of mesoporous CMS.

Author contributions

Tianshu Liu: Writing – original draft, methodology. Koki Fujita: Writing – original draft, methodology. Ayako Kawase: Conceptualization, supervision, writing – review & editing. Zheng-Ze Pan: Conceptualization, supervision, writing – review & editing. Takuma Kuroda: Conceptualization. Shinichiroh Iwamura: Methodology, supervision, writing – review & editing. Hirotomo Nishihara: Conceptualization, supervision, writing – review & editing.

Data availability

The data supporting this article have been included as part of the ESI.†

Conflicts of interest

There are no conflicts to declare.

Acknowledgements

The authors would like to express their sincere gratitude to Prof. Masayoshi Watanabe, Prof. Kaoru Dokko, and Dr Wei Yu for the valuable discussions and insightful contributions to this work. This work was supported by Council for Science, Technology and Innovation (CSTI), Cross-ministerial Strategic Innovation Promotion Program (SIP), the 3rd period of SIP "Creating a materials innovation ecosystem for industrialization" JPJ012307 (Funding agency : NIMS); and JST A-STEP Grant no. JPMJTR22T6.

References

1 Q. Li, X. Yu, H. Li and L. Chen, The road towards high-energy-density batteries, *Innovation Energy*, 2024, **1**(1), 100005.
2 H. Ando, K. Hashi, S. Ohki, Y. Hatakeyama, Y. Nishina, N. Kowata, *et al.*, State change of Na clusters in hard carbon electrodes and increased capacity for Na-ion batteries achieved by heteroatom doping, *Carbon Trends*, 2024, **16**, 100387.
3 Y. Ito, C. Lee, Y. Miyahara, K. Miyazaki and T. Abe, Operando Raman Spectroscopy Insights into the Electrochemical Formation of F-Graphite Intercalation Compounds, *ACS Energy Lett.*, 2024, **9**(4), 1473–1479.
4 W. Yu, Z. Shen, T. Yoshii, S. Iwamura, M. Ono, S. Matsuda, *et al.*, Hierarchically Porous and Minimally Stacked Graphene Cathodes for High-Performance Lithium–Oxygen Batteries, *Adv. Energy Mater.*, 2024, **14**(2), 2303055.
5 Y. Hatakeyama, H. Naito, R. Oda and S. Shiraishi, Investigation of the effect of load weight on the discharge capacity of lithium–O2 batteries using carbon-paper–based electrodes, *J. Energy Storage*, 2024, **91**, 111974.
6 Z. W. Seh, Y. Sun, Q. Zhang and Y. Cui, Designing high-energy lithium-sulfur batteries, *Chem. Soc. Rev.*, 2016, **45**, 5605–5634.
7 L. Huang, J. Li, B. Liu, Y. Li, S. Shen, S. Deng, *et al.*, Electrode Design for Lithium–Sulfur Batteries: Problems and Solutions, *Adv. Funct. Mater.*, 2020, **30**, 1910375.

8 Q. Cheng, Z. X. Chen, X. Y. Li, L. P. Hou, C. X. Bi, X. Q. Zhang, *et al.*, Constructing a 700 W h kg−1-level rechargeable lithium–sulfur pouch cell, *J. Energy Chem.*, 2023, **76**, 181–186.
9 R. Kumar, J. Liu, J. Y. Hwang and Y. K. Sun, Recent research trends in Li-S batteries, *J. Mater. Chem. A*, 2018, **6**, 11582–11605.
10 M. K. Song, E. J. Cairns and Y. Zhang, Lithium/sulfur batteries with high specific energy: Old challenges and new opportunities, *Nanoscale*, 2013, **5**(6), 2186–2204.
11 Y. W. Song, L. Shen, X. Y. Li, C. X. Zhao, J. Zhou, B. Q. Li, *et al.*, Phase equilibrium thermodynamics of lithium–sulfur batteries, *Nat. Chem. Eng.*, 2024, 588–596.
12 W. Ren, W. Ma, S. Zhang and B. Tang, Recent advances in shuttle effect inhibition for lithium sulfur batteries, *Energy Storage Mater.*, 2019, **23**, 707–732.
13 S. S. Zhang, Role of LiNO 3 in rechargeable lithium/sulfur battery, *Electrochim. Acta*, 2012, **70**, 344–348.
14 D. Aurbach, E. Pollak, R. Elazari, G. Salitra, C. S. Kelley and J. Affinito, On the Surface Chemical Aspects of Very High Energy Density, Rechargeable Li–Sulfur Batteries, *J. Electrochem. Soc.*, 2009, **156**(8), A694.
15 Z. Zhang, W. Bao, H. Lu, M. Jia, K. Xie, Y. Lai, *et al.*, Water-soluble polyacrylic acid as a binder for sulfur cathode in lithium-sulfur battery, *ECS Electrochem. Lett.*, 2012, **1**(2), A34–A37.
16 Z. Huang, L. Wang, Y. Xu, L. F. Fang, H. Li, B. K. Zhu, *et al.*, Bifunctional binder enables controllable deposition of polysulfides for high-loading Li-S battery, *Chem. Eng. J.*, 2022, **443**, 136347.
17 X. Y. Li, S. Feng, M. Zhao, C. X. Zhao, X. Chen, B. Q. Li, *et al.*, Surface Gelation on Disulfide Electrocatalysts in Lithium–Sulfur Batteries, *Angew. Chem., Int. Ed.*, 2022, **61**(7), e202114671.
18 J. Xie, B. Q. Li, H. J. Peng, Y. W. Song, M. Zhao, X. Chen, *et al.*, Implanting Atomic Cobalt within Mesoporous Carbon toward Highly Stable Lithium–Sulfur Batteries, *Adv. Mater.*, 2019, **31**(43), 1903813.
19 B. Zhang, C. Luo, G. Zhou, Z. Z. Pan, J. Ma, H. Nishihara, *et al.*, Lamellar MXene Composite Aerogels with Sandwiched Carbon Nanotubes Enable Stable Lithium–Sulfur Batteries with a High Sulfur Loading, *Adv. Funct. Mater.*, 2021, **31**(26), 2100793.
20 L. Ji, M. Rao, H. Zheng, L. Zhang, Y. Li, W. Duan, *et al.*, Graphene oxide as a sulfur immobilizer in high performance lithium/sulfur cells, *J. Am. Chem. Soc.*, 2011, **133**(46), 18522–18525.
21 B. Zhang, X. Qin, G. R. Li and X. P. Gao, Enhancement of long stability of sulfur cathode by encapsulating sulfur into micropores of carbon spheres, *Energy Environ. Sci.*, 2010, **3**(10), 1531–1537.
22 H. Wang, Y. Yang, Y. Liang, J. T. Robinson, Y. Li, A. Jackson, *et al.*, Graphene-wrapped sulfur particles as a rechargeable lithium-sulfur battery cathode material with high capacity and cycling stability, *Nano Lett.*, 2011, **11**(7), 2644–2647.
23 M. Zhao, Y. Q. Peng, B. Q. Li, X. Q. Zhang and J. Q. Huang, Regulation of carbon distribution to construct high-sulfur-content cathode in lithium–sulfur batteries, *J. Energy Chem.*, 2021, **56**, 203–208.
24 K. Ishii, T. Ogiyama, K. Fumoto and Y. Nishina, Enhanced thermal conductivity of fluids by percolating high-concentration few-layer graphene, *Appl. Phys. Lett.*, 2024, **125**(2), 023104.
25 T. Tomaru, H. Shimanoe, S. Hong, S. J. Ha, Y. P. Jeon, K. Nakabayashi, *et al.*, Preparation of spinnable mesophase pitch from pyrolyzed fuel oil by pressurized heat treatment and its application of carbon fiber, *Carbon*, 2024, **226**, 119160.
26 K. Kira, T. Yamamoto, Y. Sugimoto, I. Shimabukuro, A. Hikosaka and T. Irisawa, Improvement of carbon fiber oxidation resistance by thin ceramic coating using silica particles, *Carbon*, 2024, **228**, 119417.
27 G. Zheng, Y. Yang, J. J. Cha, S. S. Hong and Y. Cui, Hollow carbon nanofiber-encapsulated sulfur cathodes for high specific capacity rechargeable lithium batteries, *Nano Lett.*, 2011, **11**(10), 4462–4467.
28 L. Ji, M. Rao, H. Zheng, L. Zhang, Y. Li, W. Duan, *et al.*, Graphene oxide as a sulfur immobilizer in high performance lithium/sulfur cells, *J. Am. Chem. Soc.*, 2011, **133**(46), 18522–18525.
29 X. Ji, K. T. Lee and L. F. Nazar, A highly ordered nanostructured carbon-sulphur cathode for lithium-sulphur batteries, *Nat. Mater.*, 2009, **8**(6), 500–506.
30 B. Zhang, X. Qin, G. R. Li and X. P. Gao, Enhancement of long stability of sulfur cathode by encapsulating sulfur into micropores of carbon spheres, *Energy Environ. Sci.*, 2010, **3**(10), 1531–1537.
31 H. J. Peng, J. Q. Huang, X. B. Cheng and Q. Zhang, Review on High-Loading and High-Energy Lithium–Sulfur Batteries, *Adv. Energy Mater.*, 2017, **7**, 1700260.
32 J. L. Shi, C. Tang, H. J. Peng, L. Zhu, X. B. Cheng, J. Q. Huang, *et al.*, 3D Mesoporous Graphene: CVD Self-Assembly on Porous Oxide Templates and Applications in High-Stable Li-S Batteries, *Small*, 2015, **11**(39), 5243–5252.
33 X. Li, Y. Cao, W. Qi, L. V. Saraf, J. Xiao, Z. Nie, *et al.*, Optimization of mesoporous carbon structures for lithium-sulfur battery applications, *J. Mater. Chem.*, 2011, **21**(41), 16603–16610.
34 D. S. Jung, T. H. Hwang, J. H. Lee, H. Y. Koo, R. A. Shakoor, R. Kahraman, *et al.*, Hierarchical porous carbon by ultrasonic spray pyrolysis yields stable cycling in lithium-sulfur battery, *Nano Lett.*, 2014, **14**(8), 4418–4425.
35 S. Li and Z. Fan, Encapsulation methods of sulfur particles for lithium-sulfur batteries: A review, *Energy Storage Mater.*, 2021, **34**, 107–127.
36 W. G. Wang, X. Wang, L. Y. Tian, Y. L. Wang and S. H. Ye, In situ sulfur deposition route to obtain sulfur-carbon composite cathodes for lithium-sulfur batteries, *J. Mater. Chem. A*, 2014, **2**(12), 4316–4323.
37 W. Li, G. Zheng, Y. Yang, Z. W. Seh, N. Liu and Y. Cui, High-performance hollow sulfur nanostructured battery

cathode through a scalable, room temperature, one-step, bottom-up approach, *Proc. Natl. Acad. Sci. U. S. A.*, 2013, **110**(18), 7148–7153.

38 C. Wang, K. Su, W. Wan, H. Guo, H. Zhou, J. Chen, *et al.*, High sulfur loading composite wrapped by 3D nitrogen-doped graphene as a cathode material for lithium-sulfur batteries, *J. Mater. Chem. A*, 2014, **2**(14), 5018–5023.

39 A. Kawase, D. D. Han and E. J. Cairns, Low Temperature Sulfur Deposition for High-Performance Lithium/Sulfur Cells, *J. Electrochem. Soc.*, 2018, **165**(9), A1805–A1812.

40 M. K. Song, Y. Zhang and E. J. Cairns, A long-life, high-rate lithium/sulfur cell: A multifaceted approach to enhancing cell performance, *Nano Lett.*, 2013, **13**(12), 5891–5899.

41 H. Chen, C. Wang, W. Dong, W. Lu, Z. Du and L. Chen, Monodispersed sulfur nanoparticles for lithium-sulfur batteries with theoretical performance, *Nano Lett.*, 2015, **15**(1), 798–802.

42 D. Tanaka, N. Takemori, Y. Iba, K. Suyama, S. Shimizu, T. Yoshii, *et al.*, Cobalt-catalyzed carbonization from polyacrylonitrile for preparing nitrogen-containing ordered mesoporous carbon CMK-1 electrode with high electric double-layer capacitance, *Microporous Mesoporous Mater.*, 2024, **379**, 113294.

43 H. Itoi, G. Saeki, T. Usami, S. Takagi, H. Suzuki, T. Ishii, *et al.*, Activation-Free Synthesis of Chitin-Derived Porous Carbon: Application for Electrical Energy Storage, *ACS Sustainable Resour. Manage.*, 2024, **1**(4), 743–756.

44 H. Nishihara, T. Simura, S. Kobayashi, K. Nomura, R. Berenguer, M. Ito, *et al.*, Oxidation-Resistant and Elastic Mesoporous Carbon with Single-Layer Graphene Walls, *Adv. Funct. Mater.*, 2016, **26**(35), 6418–6427.

45 S. Sunahiro, K. Nomura, S. Goto, K. Kanamaru, R. Tang, M. Yamamoto, *et al.*, Synthesis of graphene mesosponge-viacatalytic methane decomposition on magnesium oxide, *J. Mater. Chem. A*, 2021, **9**(25), 14296–14308.

46 K. Kanamaru, M. Ito, M. Uchimura, Y. Ichikawa, K. Sone, A. Ikura, *et al.*, Pore-size control of soft mesoporous carbon by hot pressing, *Carbon Rep.*, 2022, **1**(4), 214–222.

47 T. Liu, R. Kaku, Z. Z. Pan, M. Ohwada, K. Pirabul, B. Li, *et al.*, Mesoporous nanoplates consisting of seamless graphene frameworks, *Electrochim. Acta*, 2024, **484**, 144034.

48 D. Blanchard and M. Slagter, In operando Raman and optical study of lithium polysulfides dissolution in lithium–sulfur cells with carrageenan binder, *J. Phys. Energy*, 2021, **3**(4), 044003.

49 L. Ji, M. Rao, H. Zheng, L. Zhang, Y. Li, W. Duan, *et al.*, Graphene oxide as a sulfur immobilizer in high performance lithium/sulfur cells, *J. Am. Chem. Soc.*, 2011, **133**(46), 18522–18525.

50 X. G. Sun, X. Wang, R. T. Mayes and S. Dai, Lithium-sulfur batteries based on nitrogen-doped carbon and an ionic-liquid electrolyte, *ChemSusChem*, 2012, **5**(10), 2079–2085.

51 C. Liang, N. J. Dudney and J. Y. Howe, Hierarchically structured sulfur/carbon nanocomposite material for high-energy lithium battery, *Chem. Mater.*, 2009, **21**(19), 4724–4730.

52 L. Ji, M. Rao, H. Zheng, L. Zhang, Y. Li, W. Duan, *et al.*, Graphene oxide as a sulfur immobilizer in high performance lithium/sulfur cells, *J. Am. Chem. Soc.*, 2011, **133**(46), 18522–18525.

53 L. Guan, H. Hu, L. Li, Y. Pan, Y. Zhu, Q. Li, *et al.*, Intrinsic Defect-Rich Hierarchically Porous Carbon Architectures Enabling Enhanced Capture and Catalytic Conversion of Polysulfides, *ACS Nano*, 2020, **14**(5), 6222–6231.

54 H. Orikasa, N. Inokuma, S. Okubo, O. Kitakami and T. Kyotani, Template synthesis of water-dispersible carbon nano "test tubes" without any post-treatment, *Chem. Mater.*, 2006, **18**(4), 1036–1040.

55 H. Nishihara, K. Imai, H. Itoi, K. Nomura, K. Takai and T. Kyotani, Formation mechanism of zeolite-templated carbons, *TANSO*, 2017, **2017**(280), 169–174.

56 J. Biscoe and B. E. Warren, An X–Ray Study of Carbon Black, *J. Appl. Phys.*, 1942, **13**(6), 364–371, DOI: **10.1063/1.1714879**.

57 W. Yu, T. Yoshii, A. Aziz, R. Tang, Z. Z. Pan, K. Inoue, *et al.*, Edge-Site-Free and Topological-Defect-Rich Carbon Cathode for High-Performance Lithium-Oxygen Batteries, *Adv. Sci.*, 2023, 2300268.

58 M. Cheng, J. Liu, H. Zhang, T. Han, M. Zhang, D. Cheng, *et al.*, A Bio-Inspired Structurally-Responsive and Polysulfides-Mobilizable Carbon/Sulfur Composite as Long-Cycling Life Li–S Battery Cathode, *ChemElectroChem*, 2019, **6**(15), 3966–3975.

59 X. Ji and L. F. Nazar, Advances in Li-S batteries, *J. Mater. Chem.*, 2010, **20**(44), 9821–9826.

60 X. Yang, X. Gao, Q. Sun, S. P. Jand, Y. Yu, Y. Zhao, *et al.*, Promoting the Transformation of Li2S2 to Li2S: Significantly Increasing Utilization of Active Materials for High-Sulfur-Loading Li–S Batteries, *Adv. Mater.*, 2019, **31**(25), 1901220.

61 F. Y. Fan and Y. M. Chiang, Electrodeposition Kinetics in Li-S Batteries: Effects of Low Electrolyte/Sulfur Ratios and Deposition Surface Composition, *J. Electrochem. Soc.*, 2017, **164**(4), A917–A922.

62 L. Kong, J. X. Chen, H. J. Peng, J. Q. Huang, W. Zhu, Q. Jin, *et al.*, Current-density dependence of Li2S/Li2S2 growth in lithium-sulfur batteries, *Energy Environ. Sci.*, 2019, **12**(10), 2976–2982.

63 Z. Shi, M. Li, J. Sun and Z. Chen, Defect Engineering for Expediting Li–S Chemistry: Strategies, Mechanisms, and Perspectives, *Adv. Energy Mater.*, 2021, **11**, 2100332.

64 C. S. Kim, A. Guerfi, P. Hovington, J. Trottier, C. Gagnon, F. Barray, *et al.*, Importance of open pore structures with mechanical integrity in designing the cathode electrode for lithium-sulfur batteries, *J. Power Sources*, 2013, **241**, 554–559.

65 H. Liu, Z. Z. Pan, A. Aziz, R. Tang, W. Lv and H. Nishihara, Nanoporous Membrane Electrodes with an Ordered Array of Hollow Giant Carbon Nanotubes, *Adv. Funct. Mater.*, 2023, **33**(40), 2303730.

66 S. Li, S. Ishikawa, J. Liu, K. Ueno, K. Dokko, G. Inoue, *et al.*, Importance of Mass Transport in High Energy Density

Lithium-Sulfur Batteries Under Lean Electrolyte Conditions, *Batteries Supercaps*, 2022, **5**(5), e202100409.

67 J. Yan, X. Liu and B. Li, Capacity fade analysis of sulfur cathodes in lithium– sulfur batteries, *Adv. Sci.*, 2016, **3**(12), 1600101.

68 Z. W. Seh, W. Li, J. J. Cha, G. Zheng, Y. Yang, M. T. McDowell, *et al.*, Sulphur-TiO 2 yolk-shell nanoarchitecture with internal void space for long-cycle lithium-sulphur batteries, *Nat. Commun.*, 2013, **4**, 1331.

69 T. Zerrin, R. Shang, B. Dong, E. C. Aguilar, J. Malvin, M. Ozkan, *et al.*, An overlooked parameter in Li-S batteries: The impact of electrolyte-to-sulfur ratio on capacity fading, *Nano Energy*, 2022, **104**, 107913.

70 A. Nakanishi, K. Ueno, D. Watanabe, Y. Ugata, Y. Matsumae, J. Liu, *et al.*, Sulfolane-Based Highly Concentrated Electrolytes of Lithium Bis(trifluoromethanesulfonyl)amide: Ionic Transport, Li-Ion Coordination, and Li-S Battery Performance, *J. Phys. Chem. C*, 2019, **123**(23), 14229–14238.

71 H. Li, J. Feng, T. Liu, K. Qin, X. Zhu and L. Suo, Suppressing sulfur crosstalk lowers the bar of lithium metal anode for practical Li-S pouch cells, *Energy Storage Mater.*, 2024, **71**, 103664.